batteries

MDPI

Article

A Comprehensive Study of Large-Format Pouch Cell Thermal Behaviour and Electrical Performance When Incorporating Cell Clamping

Xujian Zhang [1,*], Giles Prentice [2], David Ainsworth [2] and James Marco [1]

[1] Warwick Manufacturing Group, University of Warwick, Coventry CV47AL, UK; james.marco@warwick.ac.uk
[2] Castrol Technology Centre, Whitchurch Hill, Reading RG87QR, UK; giles.prentice@bp.com (G.P.); david.ainsworth@bp.com (D.A.)
* Correspondence: xujian.zhang@warwick.ac.uk

Abstract

In battery systems, external mechanical compression is commonly applied to pouch/prismatic cells to improve their electrical performance and mechanical integrity. However, cell clamping can hinder system heat rejection by introducing an additional thermal insulation layer. A novel battery clamping scheme was designed with reduced contact area to explore the system thermal behaviour under different cooling regimes. Experimental data obtained from battery characterisation and performance tests is analysed with a thermal-coupled equivalent circuit model to quantify changes in cell impedance and system thermal properties. By reducing the clamping area by 70%, the temperature rise of the cell was decreased by 0.5 °C in comparison to the reference condition of a cell with no clamping during a 1C discharge under natural convection. Under immersion cooling using BOT2100 dielectric liquid, the thermal benefit was amplified, resulting in temperature reductions of 0.9 °C at 1C and 4 °C at 3C. The principal conclusion of this work is that reshaping the clamping plate has the potential to reduce ohmic heating by lowering battery internal resistance, which outweighs the additional thermal resistance introduced by partial surface coverage. This novel experimental approach demonstrates the potential to improve battery thermal management through geometry-optimised cell clamping, particularly for high-power applications, and further directs the community towards cell clamping solution designed to optimise both thermal and mechanical cell performance.

Keywords: thermal management; lithium-ion pouch cells; cell impedance; side pressure; cell clamping; effective thermal resistance; immersion cooling

Check for updates

Academic Editor: Xianglin Li

Received: 13 March 2026
Revised: 1 April 2026
Accepted: 3 April 2026
Published: 10 April 2026

Copyright: © 2026 by the authors. Licensee MDPI, Basel, Switzerland. This article is an open access article distributed under the terms and conditions of the Creative Commons Attribution (CC BY) license.

1. Introduction

Electric vehicles (EVs) are proposed as a crucial part of the decarbonisation strategy of many developed countries. Despite their favourable fuel efficiency (circa: 86%) compared to traditional internal combustion engine (ICE) vehicles (circa: 20%) [1], range anxiety continues to hinder consumer acceptance of EVs. Fast charging has therefore attracted significant research interest as a means of improving the user experience. However, it introduces considerable technical challenges, most notably elevated cell temperature during the charge event [2]. Battery temperature crucially affects electrochemical performance, degradation rate, and operational safety, as it directly affects reaction kinetics and material stability [3]. Operating outside of the typical range (i.e., 15–35 °C [4]) causes accelerated cell capacity and power loss [5]. Generally, higher C-rates lead to greater temperature rises due

to ohmic heating, which in turn accelerates solid electrolyte interface (SEI) growth, which can lead to a further increase in cell impedance [6]. The resulting rise in overpotential reduces useable capacity during higher current excitation. During the discharge events at early stages of cell cycling, the cut-off voltage is reached sooner due to overpotential. While this effect initially limits temperature rise due to reduced discharge duration, progressive impedance growth over cycling offsets the de-rating, leading to constantly elevated operational temperatures [7]. Consequently, the increasing cell temperature accelerates degradation, including but not limited to SEI growth, electrolyte decomposition, and binder decomposition [8].

Battery electrical performance is fundamentally limited by cell impedance, which can be broadly attributed to internal resistance and polarisation resistance [9]. Internal resistance includes the internal resistance of the battery material (i.e., electrodes, electrolyte, separator, etc.), whereas polarisation resistance defines the electrochemical kinetics, electrolyte conductivity, ionic diffusion etc. [10]. While the internal resistance has been proven to typically be insensitive to the variation of temperature within the range of 10–50 °C [11], several studies illustrated the monotonic relationship between polarisation resistance components (i.e., charge transfer resistance, mass transfer resistance, etc.) and temperature within the same range [12,13]. Therefore, battery thermal management systems (BTMSs) have been widely used to regulate battery temperature, thus prolonging battery service life and enhancing cell electrical performance.

In addition to thermal effects, lithium-ion batteries undergo reversible volumetric expansion/contraction during lithium (de)intercalation, while irreversible swelling may occur due to lithium plating and the formation of gaseous products [14]. The volumetric expansion induces physical degradation mechanisms including but not limited to internal fracture and delamination of electrode layers [15]. The application of side pressure during cell integration has been acknowledged for its role in restraining physical deformation of electrode materials, thereby mitigating internal fracture during cycling [16]. Numerous studies highlight that applying an external mechanical force to pouch/prismatic cells improves capacity retention in cell cycling due to improved mechanical integrity [17,18]. Moreover, its effect on cell impedance was also recognised and extensively reviewed in the study of Müller et al. [19]. It was demonstrated that the electrical contact between the electrode materials of a pouch/prismatic cell is enhanced when side pressure is applied, thereby reducing internal resistance [20]. This finding was affirmed by Berckmans et al. [21], who further concluded that side pressure increases usable cell capacity from reduced overpotential. Du et al. extended their findings by linking the reduction in cell impedance to lower heat generation rates of a large-format NMC pouch cell via Joule heating, concluding that the application of side pressure reduces heat generation [22].

Based on the literature, incorporating cell clamping into battery pack designs may simultaneously enhance mechanical integrity, electrical performance, and thermal behaviour. However, existing studies have predominantly focused on electrical performance and ageing benefits under uniform full-area clamping. In addition, the additional thermal resistance associated with compromised heat rejection has received limited attention. To the best of the authors' knowledge, the closest attempt was the deployment of heat flux sensors between a cell clamping system and a large-format pouch cell by Du et al. [22]. To address this gap, a bespoke clamping scheme was introduced to partially constrain the cell in addition to a conventional solid clamping architecture commonly used in prominent studies. Surface temperature measurements were obtained via thermocouples embedded within the clamping plate design, enabling representative thermal characterisation without damaging the pouch material. By combining battery characterisation, performance testing, and thermally coupled equivalent circuit modelling, the effects of the bespoke

cell clamping scheme on battery heat generation, heat rejection, and the resulting thermal management requirements are quantified. This work contributes to a novel perspective of cell clamping system design which simultaneously enhances electrical, thermal, and mechanical performance.

This paper is structured as follows. The experimental methodology is presented in Section 2, including the design of cell clamping fixtures and experimental methodology employed. Experimental and simulation results are discussed separately in Section 3 and Section 4, respectively. The Discussion and Conclusions are presented in Section 4 and Section 5, respectively.

2. Experimental Methodology

To investigate the effect of cell clamping area on battery thermal behaviour, three cell clamping configurations were designed and fabricated with 10 mm Perspex sheets to cover 0%, 30% and 100% of the test cell surfaces, denoted as "Unclamp", "Bespoke", and "FullClamp" configurations, respectively, as shown in Figure 1. For "Bespoke" and "FullClamp" arrangements, a total clamping force of 900 N was applied by ten spring-driven bolts, corresponding to an equivalent average pressure of 30 kPa between electrode layers. The detailed clamping setup parameters can be found in our previous work [23] and are therefore not repeated here. The "Bespoke" clamping plate was intentionally designed to avoid the major hot regions (i.e., areas close to the tabs) based on thermal images captured during trial tests and retain a relatively uniform pressure pattern, which primarily serves as a proof-of-concept prototype rather than an optimised design. The thermal images are further discussed in Section 3.1. The ratio of 30% clamping coverage was the minimal clamping area required to avoid exceeding the recommended pressure range at local areas when subjected to the same mechanical force. As reported in the literature [24,25], large-format NMC pouch cells typically exhibit modest temperature rise with natural convection, ranging from 5 to 8 °C at a 1C discharge rate. Compared with materials of higher thermal conductivities (e.g., aluminium: 237 W/mK [26]), the material choice of Perspex (circa: 0.19 W/mK [27]) was both for ease of manufacture in the system design and to intentionally amplify discrepancies in thermal response between clamping configurations, thereby avoiding overlap in measured temperature behaviour.

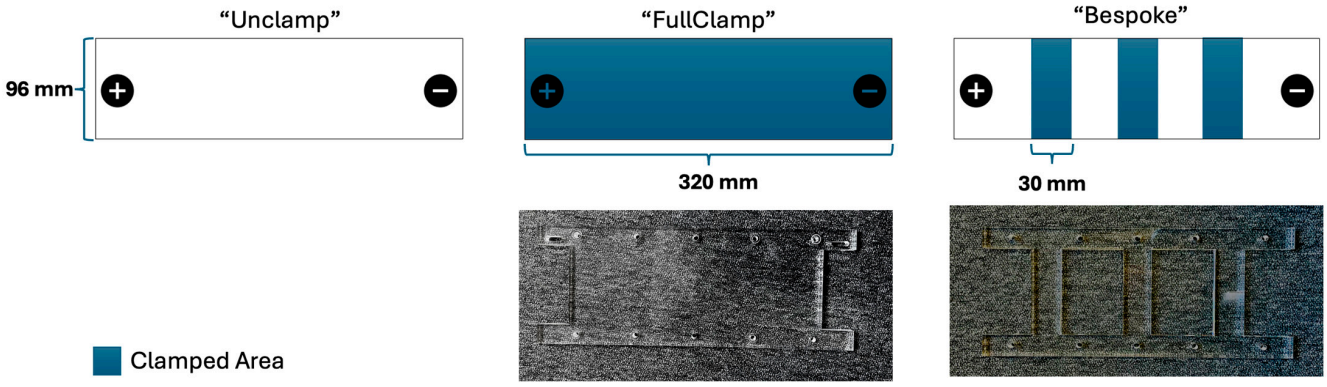


Figure 1. The fabricated clamping plates and the scheme of applied mechanical pressure.

Large-format pouch cells from an electric–global modular platform used by Hyundai and KIA UK (SK 55.6 Ah NMC811 battery) were selected for this study, and the specification is presented in Table 1. In the original battery pack configuration, thermal management is achieved via indirect cooling using an aluminium cold plate with minimal surface contact, which is sufficient for the relatively low average current demand of standard EV driving cycles (typically below 0.2C for the WLTC cycle [28]). To extend the applicability of this

study, the cells were tested up to the maximum C-rate (i.e., 3C) recommended by the manufacturer. In addition to ambient conditions, an immersion cooling environment was implemented to enable a comparison of the battery thermal response under cooling regimes with different heat exchange rates.

Table 1. Specification of SK E556 battery.

Upper cut-off voltage	4.16 V
Lower cut-off voltage	3 V
Battery dimension	320 mm × 96 mm × 10 mm
Weight	0.75 kg
Chemistry	NMC 811
Capacity	55.6 Ah
Nominal voltage	3.7 V
Maximum C-rate allowed	3C
Recommended Pressure	24–128 kPa

2.1. Thermocouple Instrumentation

The battery thermal behaviour was measured with K-type thermocouples instrumented into the clamping plates and in direct contact with the cell surface. Identical sensor locations were maintained across all clamping configurations and experimental work to enable direct comparison of local temperature responses under different clamping schemes. As directly placing thermocouples between the pouch cell surface and the Perspex sheet creates high local pressure while applying external mechanical force, it is vital to prevent the potential damage of the pouch material which can subsequently lead to electrolyte leakage. For each thermocouple instrumented into the clamping arrangements, a 2 mm wide slot was machined to accommodate the additional wiring. A thin layer of Kapton tape was applied after embedding the thermocouple, leaving a minimal sensing area in direct contact with the pouch cell surface. This approach reduces the likelihood of sharp edge finishes in the machining process that could damage the pouch material. For cells tested without external cell clamping applied, thermocouples were directly affixed to the pouch surface using Kapton tape. The thermocouple measurement data were collected with Pico Loggers operating at a 1 Hz sampling rate. To capture the representative battery thermal behaviour, a detailed sensor deployment scheme was applied based on thermal images observed with a Teledyne forward-looking infrared (FLIR) C2 camera. A direct comparison of thermal profiles was made between the "Unclamp" and "FullClamp" arrangements which is further discussed in Section 3.1.

2.2. Experimental Setup

The electrical tabs located on both sides of the cell were connected to the cycler channels through bespoke brass blocks. Charging and discharging were performed using a single-range Bitrode MCV cycler (0–5 V, ±100 A per channel, ±0.1%F.S.). The cycler recorded current, terminal voltage, and temperature (measured with the channel T-type thermocouple for safety monitoring) at a rate of 1 Hz.

As shown in Figure 2, the ambient environment was established using an ESPEC thermal chamber. An immersion cooling environment was implemented by placing the test rig inside a sealed container filled with Castrol BOT2100 thermal management fluid (specific heat capacity: 2.1–2.3 kJ/kgK at 20–60 °C operation temperature), where a heat exchanger was placed and connected to a Lauda unit. The Lauda unit provides closed-loop

temperature control by circulating water/glycol inside the heat exchanger at varying flow rates, which indirectly controls fluid temperature. To avoid the formation of localised hot regions in a static fluid environment, two FT-350 electric pumps (flow rate: 350 L/h) were also immersed in the lubricant to create turbulence. The temperature for both cooling environments was maintained at 25 °C. In the immersion cooling setup, the tabs of test cells were extended to the top of the container with additional power cables to allow operation within the enclosed container. As additional wiring introduces extra ohmic resistance, it affects battery electrical performance due to higher overpotential especially at higher C-rates. To eliminate the influence of lead and contact resistance, a four-point electrical connection [28,29] was made between the cycler and the cells under test. This technique separates the voltage sensor of each cycler channel from the power cable and directly attaches it to the respective battery tab, which was adopted in the immersion cooling setup.

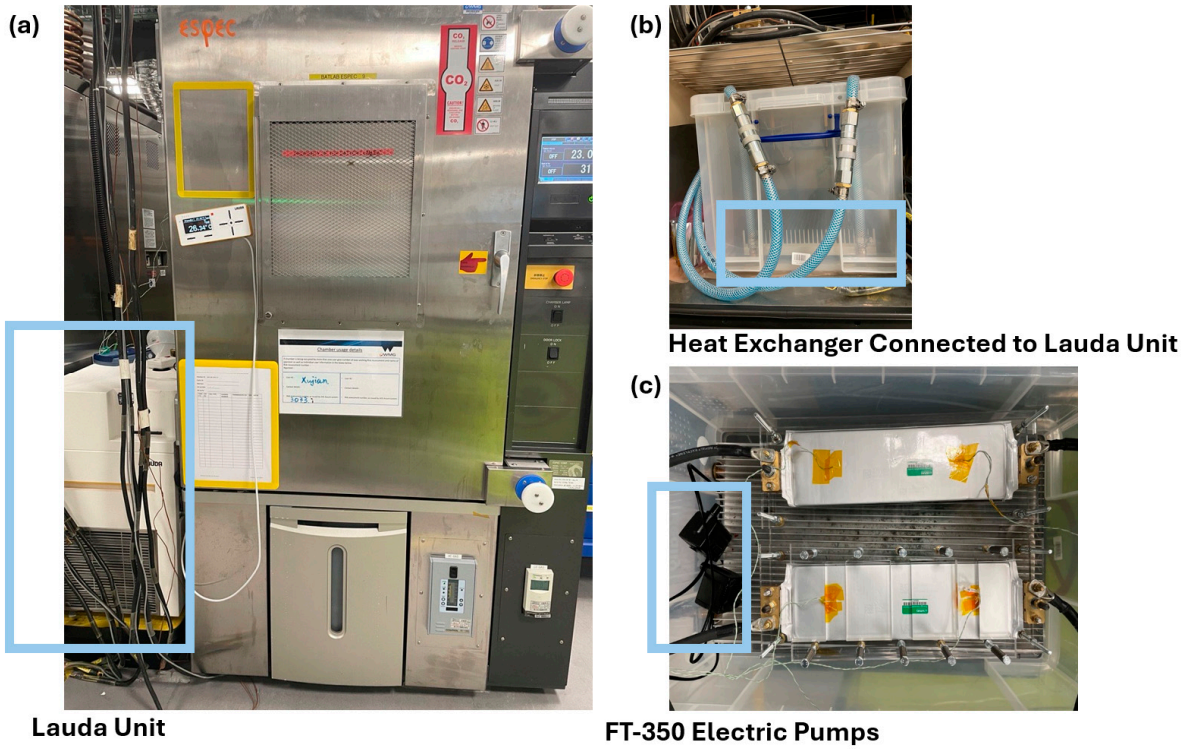


Figure 2. Experiment equipment setup: (**a**) thermal chamber and Lauda unit; (**b**) immersion cooling setup and the connection to Lauda unit; (**c**) cell clamping arrangement in the immersion cooling environment.

2.3. Test Techniques

As identified from the literature [22], the thermal benefits of cell clamping originate mainly from the reduced ohmic resistance via improved electrical contact. To characterise the corresponding changes in cell impedance, hybrid pulse power characterisation (HPPC) and electrochemical impedance spectroscopy (EIS) techniques were employed.

For HPPC, the cell was initially charged using a 1C (55.6 A) constant current–constant voltage (CC-CV) protocol. The cell was charged at 55.6 A until reaching the constant-voltage phase (4.16 V), which was terminated when the current dropped below C/20 (2.7 A) at 4.16 V. The pulse characterisation was conducted at 10% state-of-charge (SOC) intervals, and the battery SOC was adjusted at 0.2C (11.1 A) with a 1 h rest period to allow equilibrium. At each target SOC, the cell was subject to 30 s of 0.2C (11.1 A) and 1C (55.6 A) discharge pulses with 20 min of relaxation. The discharged energy was compensated at 0.2C (11.A) with the same relaxation time. The current profile of this technique is shown in Figure 3a.

It is noteworthy that the sampling rate of HPPC was constrained to 10 Hz (the highest sampling rate available on the Bitrode cycler). Besides the instantaneous voltage drop, partial logarithmic voltage dynamics were captured [30]. Consequently, the resultant value represents the average value of internal resistances calculated from different current pulses.

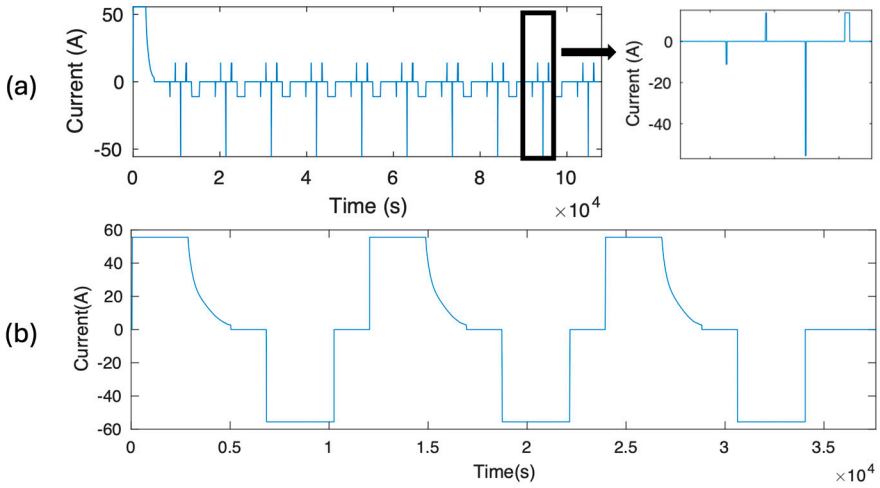


Figure 3. Current profiles of (**a**) HPPC and (**b**) the constant C-rate discharge test.

For EIS, the cell was initially fully charged using the 1C CC-CV charging protocol as defined above. Following a rest period of 30 min, the cell was discharged to 50% SOC at 0.2C (11 A) and subjected to a rest period of 30 min before each EIS assessment. The EIS test device used was a Biologic BSC-815 cycler (accuracy: ±0.05% of value). At 50% SOC, the cell was tested in potentiostatic mode (sinusoidal amplitude: 10 mV) at a 33 mHz–1 kHz frequency range. To avoid discrepancies arising from environmental variation and operator procedure, all EIS tests were repeated three times with a 30 min rest period in between, and the result was accepted only when there were no significant discrepancies (i.e., average error $\leq$ 0.1%) between the Nyquist plots.

In addition to cell characterisation techniques, a constant C-rate discharge test was incorporated as a standard procedure to measure battery thermal behaviour at different C-rates. After thermally stabilising for 1 h in the respective cooling environment, the cell was charged using the 1C CC-CV charging protocol defined above and then discharged at 1C until the cut-off voltage of 3 V was reached. To mitigate causality in experimental results, each constant C-rate discharge test was repeated three times with a 30 min rest period prior to the next cycle, as shown in Figure 3b. For higher C-rate tests, the excitation was adjusted accordingly up to ±166.8 A, corresponding to 3C operation.

3. Experimental Results

3.1. Thermal Profile

The representative thermal profiles of the test cell are presented in Figure 4a,b. Under constant current loading, elevated temperatures were observed in regions close to the current collector tabs and in the central area of the pouch cell. During the subsequent rest period, the central region remained the dominant localised hot spot, consistent with comparatively slower heat dissipation in this area. Based on these observations, thermocouple deployment locations were selected to capture representative thermal profiles, as shown in Figure 4c and Figure 4d for the "Unclamp" and "FullClamp" arrangements, respectively.

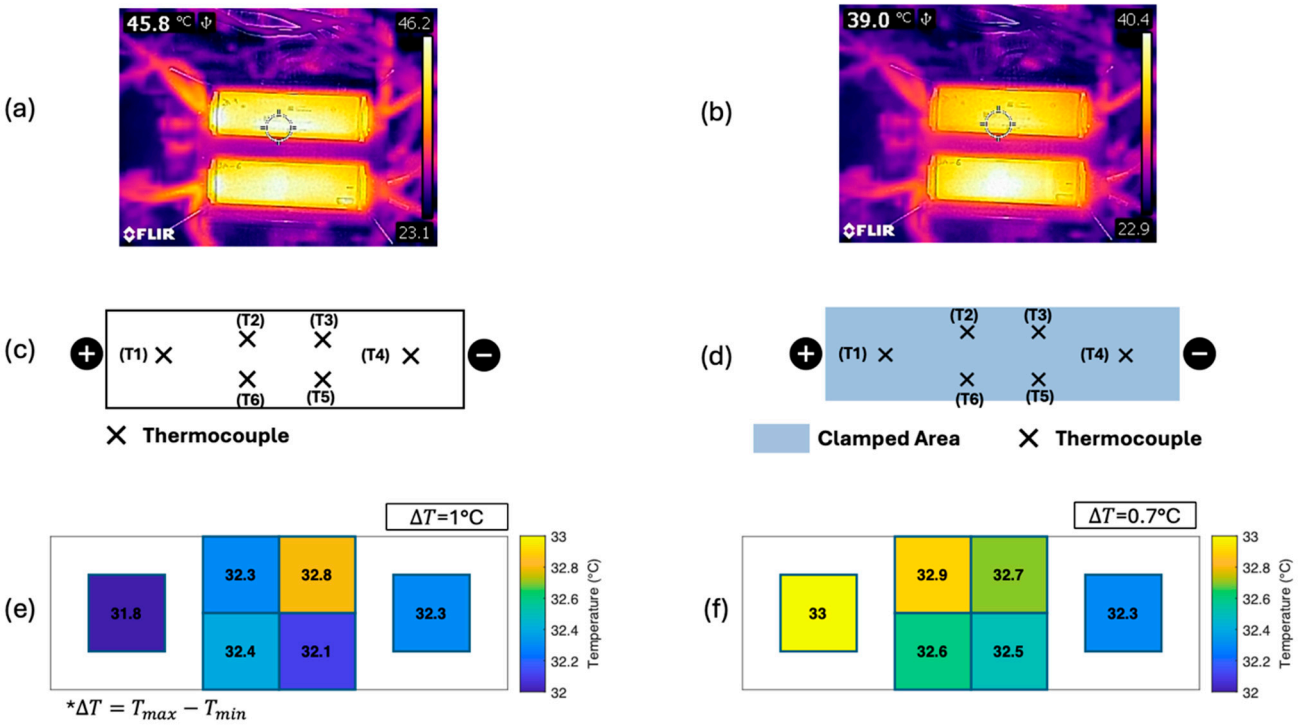


Figure 4. Thermal images of the test cell captured at (**a**) the end of a 3C CC charge and (**b**) rest interval; thermocouple deployment schemes of (**c**) "Unclamp" arrangement and (**d**) "FullClamp" arrangement; measured thermal profiles at the end of 1C CC charge under (**e**) "Unclamp" arrangement and (**f**) "FullClamp" arrangement.

Peak surface temperature profiles measured using thermocouples during a 1C CC-CV charge are presented in Figure 4e,f. Under the "Unclamp" arrangement, the test cell exhibited minimal in-plane thermal gradients (denoted ΔT) of 1 °C, which is in line with values widely identified in the literature [24]. However, the localised hot region occurred at Location 3, which deviates from typical observations in existing studies where T1 (i.e., the region closest to the positive tab) tends to exhibit the highest temperature rise [31]. Conversely, the maximum cell temperature occurred at Location 1 when subjecting the test cell to the "FullClamp" arrangement, as shown in Figure 4f. The misalignment discovered in Figure 4e was likely due to the orientation of the test cell in the chamber, where the forced air flow outlet was closer to the positive tab of the battery and caused uneven heat removal on the cell surface. This assumption was validated by repeating the ambient condition test in an enclosed container with minimal air flow, and the thermal profile agreed with Figure 4f. Therefore, the thermal profile from the "FullClamp" arrangement in Figure 4f is more representative. The in-plane thermal gradient (ΔT) of the test cell under the "FullClamp" arrangement is 0.7 °C, indicating that the homogenous cell clamping scheme does not amplify variations in battery thermal profiles. For T3 and T4, cell temperatures did not vary notably despite being covered by an additional Perspex sheet, which confirms the thermal benefits of cell clamping by reducing heat generation. In contrast, cell temperature increases were observed at the other locations, which may be associated with the additional thermal resistance introduced by the clamping plate and local variation in electrical contact under cell clamping. Based on the captured thermal profiles, T1 and T4 consistently represent the maximum and minimum cell temperatures that define the in-plane thermal gradient. Therefore, the following sections primarily focus on the battery thermal behaviour at these two locations.

3.2. Temperature Rise

Following the constant C-rate discharge defined in Section 2, the temperature data measured by T1 under different clamping arrangements are presented in Figure 5. As the experimental results from three test cells were consistent and showed minimal differences (i.e., less than 0.2 °C, which is within the K-type thermocouple accuracy of ±0.75%) in temperature rises, the presented data is of one cell for clarity. In the ambient environment, the "FullClamp" configuration led to a notable increase of over 1 °C in cell peak temperature compared to the "Unclamp" arrangement. In addition, while cell temperature measured under the "Unclamp" and "Bespoke" configurations returned to environment temperature (i.e., 25 °C) after each charge/discharge event, that of the "FullClamp" configuration was consistently above 27 °C despite the 30 min rest period prior to the next cycle. Conversely, the "Bespoke" configuration did not appear to affect the heat rejection and resulted in a 0.5 °C decrease in temperature rise compared to the "Unclamp" assembly. The hierarchy of cell temperature under different clamping arrangements was consistent in both ambient and immersion cooling environments. Under immersion cooling, the "Bespoke" setup further reduced the peak cell temperature by 0.9 °C compared with the "Unclamp" condition. Temperature measurements were repeatable over three consecutive cycles, and the thermocouples remained in direct contact with the pouch surface throughout testing, supporting the robustness of the observed temperature hierarchy.

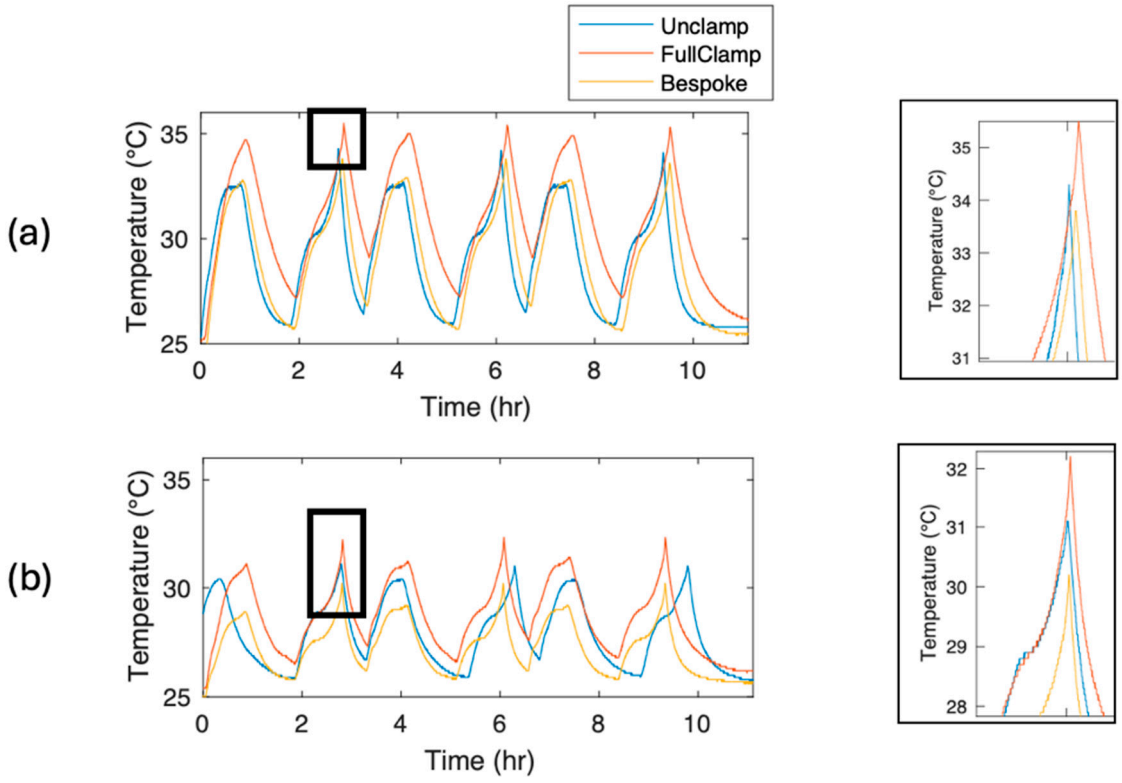


Figure 5. The experimental result of temperature rise with different cell clamping setups in the (**a**) ambient environment and (**b**) immersion cooling environment.

To examine the thermal benefits of the "Bespoke" arrangement at higher C-rates, Figure 6 presents the temperature data measured at Location 1 and Location 4 (the highest and lowest temperature points, as discussed in Section 3.1, denoted as $TU1/TB1$ and $TU4/TB4$) at 1–3C. The maximum temperature values in the boxed areas are tabulated in Tables 2 and 3. In the ambient environment, temperature differences between the "Unclamp" and "Bespoke" arrangements at Location 1 were small at 1C but increased

progressively as higher C-rates were applied, reaching 1.1 °C, 1.6 °C, and 1.8 °C at 2C, 2.5C, and 3C, respectively. The corresponding differences at Location 4 were 0.5 °C, 1.5 °C, 1 °C, and 2 °C across the same C-rates. The increasing separation at higher C-rates is consistent with trends reported in the literature for impedance-related heat generation [32].

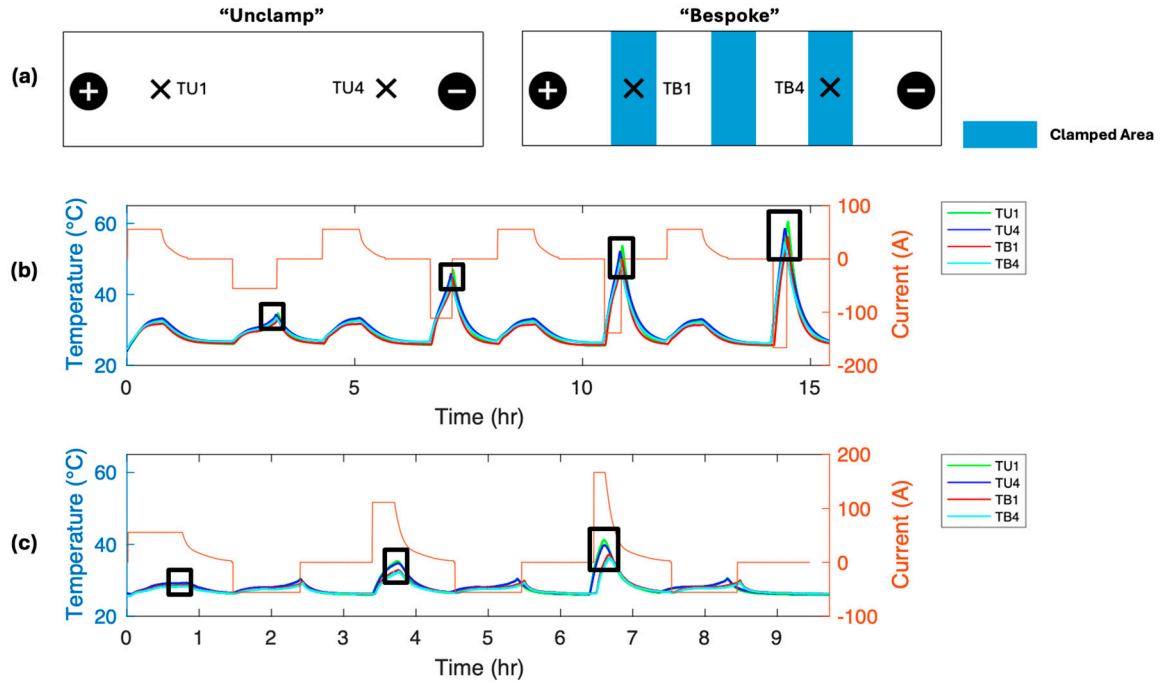


Figure 6. (**a**) Denotation of temperature data; (**b**) temperature rise of 1C, 2C, 2.5C and 3C discharge in the ambient environment; (**c**) temperature rise of 1C, 2C, and 3C CC-CV charge in the immersion cooling environment.

Table 2. The peak temperature values corresponding to Figure 6b.

Discharge C-Rate	1C	2C	2.5C	3C
TU1 (°C)	34.6	46.9	53.6	60.3
TU4 (°C)	33.3	43.9	49.8	56.2
TB1 (°C)	34.3	45.8	52.0	58.5
TB4 (°C)	33.4	43.4	48.8	54.2

Table 3. The peak temperature values corresponding to Figure 6c.

Charge C-Rate	1C	2C	3C
TU1 (°C)	29.2	35.3	41.2
TU4 (°C)	29.4	34.8	39.8
TB1 (°C)	28.7	32.9	37.1
TB4 (°C)	28.4	32.5	36.4

When submerging the test rig in the cooling fluid, the temperature reduction associated with the "Bespoke" configuration became more pronounced at elevated C-rates, as highlighted in Figure 6c. At Location 1, the "Bespoke" arrangement reduced cell temperature by 0.5°, 2.4 °C and 4.1 °C at 1C, 2C and 3C, respectively, relative to the "Unclamp" arrangement. At Location 4, the corresponding reductions were 1 °C, 2.3 °C, and 3.4 °C. Compared with the ambient environment, the magnitude of temperature reduction under

immersion cooling increased substantially at 2C and 3C. This enhancement was expected as the reduced heat generation from cell clamping (i.e., a function of current profile and battery ohmic resistance) was asserted to be constant, assuming minimal differences in battery electrical performance and characteristics in different cooling environments due to insignificant temperature differences (as shown in Figure 5); this was more pronounced with a lower battery heat gain when placed in a more effective cooling environment.

The in-plane thermal gradients defined by ΔTU (i.e., $TU1 - TU4$) and ΔTB (i.e., $TB1 - TB4$) under the "Unclamp" and "FullClamp" arrangements both increased at higher C-rates, as widely reported in relevant studies [31]. The incorporation of the "Bespoke" cell clamping scheme did not impact the thermal gradients in the ambient ($\Delta TU = 4.1$ °C, $\Delta TB = 4.3$ °C) and immersion cooling environments ($\Delta TU = 1.4$ °C, $\Delta TB = 0.7$ °C). This finding agrees with previous results in Section 3.1, where the "FullClamp" arrangement did not significantly affect the thermal gradients on the test cell at 1C, although the thermal profile may vary depending on the geometry of the clamping plate design.

In addition to thermal behaviour, reductions in overpotential associated with lower internal resistance under the "Bespoke" configuration influenced electrical performance. Therefore, the corresponding constant-current discharge capacity and charge capacity from tests shown in Figure 6 are tabulated in Tables 4 and 5 for completeness. In alignment with the trends identified in the previous temperature data, incorporating the "Bespoke" clamping scheme enhanced cell electrical performance, especially at higher C-rates, increasing the discharge capacity and CC charged capacity by 1.1 Ah and 3.4 Ah at 3C. This result further demonstrates the benefits of reduced internal resistance under cell clamping, which improved battery thermal behaviour despite the extended period of higher current loading. The benefits tend to be more pronounced in an efficient cooling environment and at higher C-rates.

Table 4. Battery discharge capacity corresponding to Figure 6b.

Discharge Capacity (Ah)	1C	2C	2.5C	3C
Unclamp	53.8	52.7	51.3	48.9
Bespoke	54.1	52.9	51.7	50.0

Table 5. Battery charged capacity during CC phase corresponding to Figure 6c.

C-Rate	Clamping Setup	CC Phase Charged Capacity (Ah)
1C	**Bespoke**	41.5
	Unclamp	41.9
2C	**Bespoke**	36.4
	Unclamp	34.2
3C	**Bespoke**	29.4
	Unclamp	26.0

3.3. Cell Impedance

Following the HPPC procedure described in Section 2.3, the internal resistances characterised from three test cells under different clamping schemes are shown in Figure 7a. The variation in internal resistance under the same clamping arrangement was minimal, exhibiting a clear hierarchy of battery internal resistance measurements. A uniform side pressure ("FullClamp") resulted in a greater reduction in internal resistance ranging from 0.1 mΩ to 0.2 mΩ (average 10.5%) compared to the "Bespoke" cell clamping setup (average

3.6%) when applying the same mechanical force. This result aligns with the relationship between side pressure and electrical contact presented by Müller et al. [19], as the unevenly distributed side pressure causes uneven electrical contact especially in the unclamped areas. The rate of internal resistance reduction agrees with the design of the "Bespoke" clamping plate with reduced clamping area (28.1% coverage), suggesting that applying a mechanical force on a larger surface area (in addition to the Bespoke clamping plate geometric design) would enhance electrical contact and consequently further reduce internal resistance.

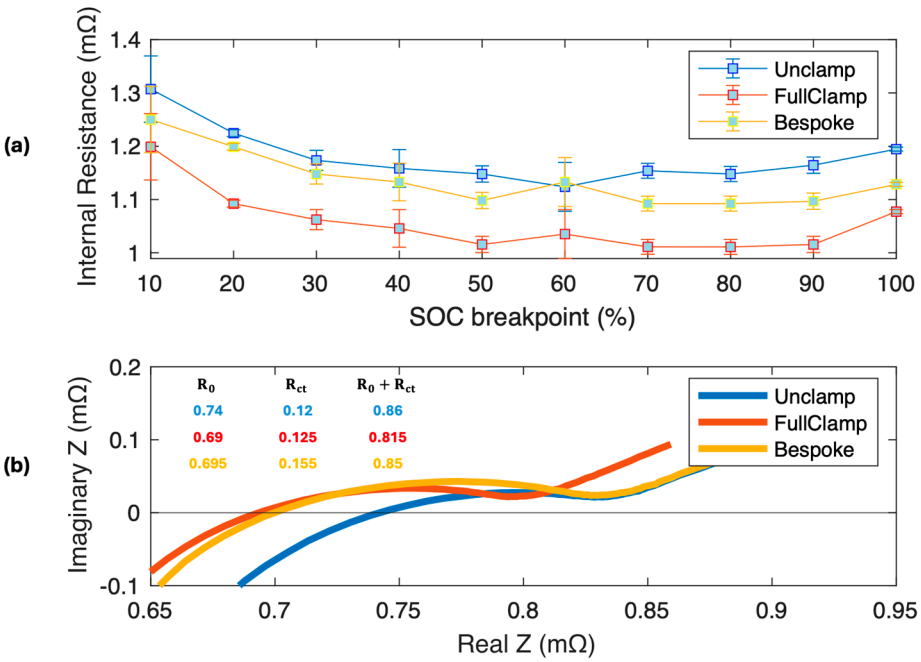


Figure 7. Experimental results of (**a**) HPPC and (**b**) EIS under different cell clamping arrangements.

As addressed previously in Section 2.3, the characterised cell internal resistance contains partial "imaginary impedance" at a 10 Hz sampling rate limited by the cycler; therefore, EIS was employed to further resolve the cell impedance response. Since the characterisation results showed minimal differences between the test cells, the Nyquist plot of only one test cell at 50% SOC is presented in Figure 7b for clarity. As expected, the characterised ohmic resistances were lower than those from HPPC at 50% SOC due to the exclusion of charge transfer impedance, although the hierarchy of ohmic resistance between different cell clamping arrangements is consistent from both techniques. According to a comparison study of internal resistance measurements between EIS and HPPC established by Barai et al. [33], different characterisation techniques were in agreement when compared at the same timescale, although EIS measurement was the closest to the true internal resistance. In addition, the discrepancies of internal resistance between EIS and HPPC were also partially affected by the electrical connection of different cyclers; therefore, the result is only reviewed comparatively within the EIS test.

The "FullClamp" arrangement resulted in a reduction of 0.05 mΩ compared to the "Unclamp" setup, corresponding to 7% of the total ohmic resistance. The "Bespoke" setup also resulted in a similar reduction in internal resistance of 0.045 mΩ. The insignificant impact of both cell clamping arrangements on cell resistance can be attributed to the pristine state of the test cells with minimal discrepancies in regional electrical contact. While cell clamping showed clear benefits in internal resistance (R_0), the charge transfer resistance (i.e., the second cross-over with x-axis by extending the semi sphere, denoted R_{ct}) appeared to be compromised. The "Bespoke" clamping arrangement caused an increase of 0.035 mΩ in R_{ct}, whereas the "FullClamp" configuration resulted in a marginal increase of 0.005 mΩ.

Given the clamping parameter setup, where the same mechanical force was applied on both clamping plates regardless of clamping areas, the "Bespoke" configuration would result in a higher regional pressure (circa: 100 kPa) on the test cell. According to relevant studies, the contact between the electrode layers and electrolyte (i.e., wettability) of the battery is improved when incorporating cell clamping [17]. However, Du et al. addressed that an overly high pressure could cause reduced anode porosity, which compromises the ionic diffusion capability, where the R_{ct} of a large-format pouch cell exhibited a monotonically increasing trend with increasing mechanical pressure ranging from 30 to 310 kPa [22]. Therefore, the external mechanical force applied to cell clamping systems with reduced clamping area must be carefully considered to avoid excessively increasing R_{ct}. Despite the increase in R_{ct}, the "Bespoke" clamping setup still reduced the overall impedance ($R_0 + R_{ct}$) compared to the "Unclamp" test group.

As the pristine test cells exhibited insignificant differences in cell impedance under cell clamping, we characterised three other SK 55.6 Ah NMC pouch cells removed from a KIA EV6 battery pack with approximately four years of service time. All cells had over 90% cycle capacity retention without significant bulking (thickness ranging from 10 to 10.3 mm, with that of the pristine state being 9.8–10 mm for the test cells used in the study). Due to different degrees of degradation, these cells were not employed in the performance test. Instead, these cells were subject to EIS at 20%, 50%, and 80% SOC under different clamping schemes for completeness of this section.

As shown in Figure 8, Cell 2 and Cell 3 agree with the previous result, where the "FullClamp" setup exhibited a greater reduction in internal resistance than the "Bespoke" arrangement. In contrast, the EIS result of Cell 1 showed an opposite trend, most notably at 50% SOC. The internal resistance of Cell 1 increased under both cell clamping setups. This feature is aligned with the HPPC result presented in Figure 7a, where the application of side pressure caused an overshoot at 50–60% SOC compared to the R_0 measured for the unclamped condition. While other studies have reported reduced internal resistance under similar side pressure conditions for NMC pouch cells of various sizes/capacities (e.g., 1.4 Ah NMC622 pouch cell by Müller et al., [19], and 101.8 Ah NMC811 pouch cell by Du et al. [22]), our findings on Cell 1 are more consistent with the work of Barai et al. [17], who applied 15 psi (circa: 103 kPa) side pressure on a 15 Ah NMC pouch cell and attributed the increased internal resistance to the reduced ionic conductivity from separator deformation. A similar conclusion was made by Cannarella et al. [34], although the objects were bespoke cells assembled with separators from commercialised batteries. These findings suggest that the overshoot behaviour at mid-range SOC is less dependent on cell size or capacity and may instead arise from intrinsic cell-to-cell variability, warranting further investigation.

The R_0 and R_{ct} values of Figure 8 are tabulated in Table 6. When comparing R_0 between "Unclamp" and "FullClamp" arrangements within the test cells, the difference in R_0 seems insensitive to varying SOCs with ΔR_0 being -0.05 mΩ (as cell clamping increased R_0 for Cell 1 instead), 0.4 mΩ, and 0.35 mΩ for Cell 1, Cell 2, and Cell 3, respectively. As identified in the literature [14], lithium-ion batteries undergo volumetric expansion during the charging process due to lithium intercalation and thermal expansion, which means the mechanical pressure applied on the pouch cell increases at higher SOCs due to battery bulking. This suggests the optimal internal resistance for this type of test cell can be achieved at a relatively low homogeneous pressure (30 kPa in our study), which agrees with experimental results from the literature [22], where a large-format NMC pouch cell exhibited less than 0.01 mΩ variation in internal resistance under a mechanical pressure ranging from 30 to 310 kPa. The "Bespoke" configuration did not show a consistent reduction in internal resistance between different test cells, which may arise from the occurrence of local degradation, which varies between different test cells.

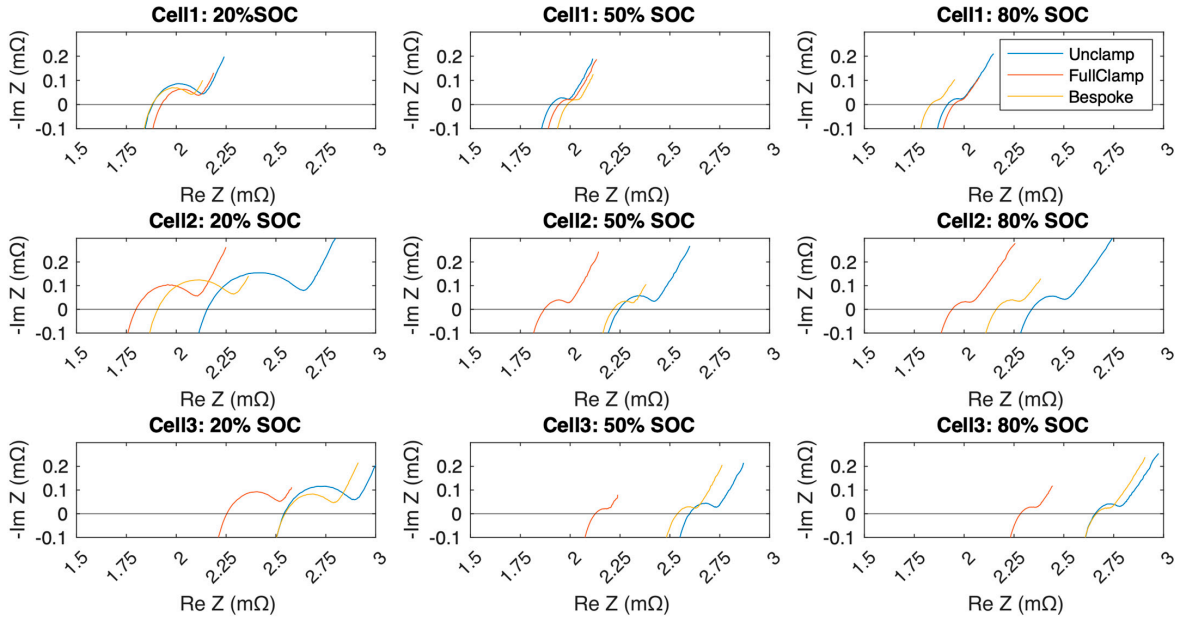


Figure 8. EIS results of used SK E556 batteries.

Table 6. Cell impedance values corresponding to Figure 8 (mΩ).

Cell 1	**20% SOC**		**50% SOC**		**80% SOC**	
	R_0	R_{ct}	R_0	R_{ct}	R_0	R_{ct}
Unclamp	1.8	0.4	1.9	0.15	1.9	0.15
FullClamp	1.9	0.25	1.95	0.15	1.95	0.15
Bespoke	1.8	0.3	2	0.15	1.8	0.25
Cell 2	**20% SOC**		**50% SOC**		**80% SOC**	
	R_0	R_{ct}	R_0	R_{ct}	R_0	R_{ct}
Unclamp	2.15	0.55	2.25	0.2	2.35	0.2
FullClamp	1.75	0.4	1.85	0.2	1.95	0.15
Bespoke	1.9	0.5	2.2	0.15	2.15	0.2
Cell 3	**20% SOC**		**50% SOC**		**80% SOC**	
	R_0	R_{ct}	R_0	R_{ct}	R_0	R_{ct}
Unclamp	2.55	0.4	2.6	0.2	2.65	0.2
FullClamp	2.25	0.3	2.15	0.15	2.3	0.1
Bespoke	2.55	0.3	2.55	0.25	2.65	0.15

The previous EIS results on pristine cells suggested that cell clamping increased the R_{ct}. Nonetheless, the characterisation results of the aged cells presented the opposite phenomenon: the "FullClamp" setup reduced R_{ct} by 0.05–0.15 mΩ for all test cells, whereas the "Bespoke" arrangement, despite creating high local pressure, reduced R_{ct} by 0–0.1 mΩ. The reduction in charge transfer resistance due to side pressure aligns with previous studies [17,19], which highlighted that the cell clamping configuration improved the wettability, thereby reducing charge transfer impedance. As there appear to be thickness differences between pristine and KIA EV6 batteries as stated above, the change in R_{ct} may arise from the irreversible battery swelling caused by gas generation and lithium plating at a higher degree of degradation, which would create delamination between electrode materials. In contrast to the insignificant response of R_0 to varying SOCs, R_{ct} appeared to be more

pronounced at 20% SOC, where the greatest reduction in R_{ct} was observed under both the "FullClamp" (0.1–0.15 mΩ across the cells) and "Bespoke" (0.05–0.1 mΩ across the cells) arrangements. Comparatively, cell clamping had minimal impact on R_{ct} at 50% and 80% SOC, with a maximum reduction of 0.05 mΩ for both clamping arrangements.

Table 7 collates a qualitative summary of the cell characterisation data of the aged cells discussed above. Combined with the results from the pristine cells, homogenous side pressure appears to be most effective in reducing total cell impedance (i.e., $R_0 + R_{ct}$), particularly for aged cells. While both clamping schemes exhibited relatively consistent reduction in R_0 across different SOCs, the reduction in R_{ct} seems to be more pronounced at a low SOC. The "Bespoke" arrangement provided more variable impedance reductions, with cell-to-cell differences becoming more pronounced at a higher level of degradation.

Table 7. Qualitative summary of the effect of the cell clamping schemes on cell impedance components of the aged cells.

Cell SOC		20% SOC	50% SOC	80% SOC
"FullClamp"	R_0	Higher	Higher	Higher
	R_{ct}	Moderate	Lower	Lower
"Bespoke"	R_0	Moderate	Moderate	Moderate
	R_{ct}	Moderate	Lower	Lower

Lower: 0–0.05 mΩ; moderate: 0.05–0.2 mΩ; higher: >0.2 mΩ.

4. System Thermal Resistance

4.1. Mathematical Modelling and Parameters

Battery temperature rise can be broadly considered a result of both battery heat generation and heat rejection. The previous section presented the positive effect of cell clamping on cell impedance and extended thermal benefits via reduced heat generation. To understand the potential trade-off between improved battery characteristics and impeded system heat rejection, this section quantifies and discusses the resultant system thermal resistances under the same three clamping arrangements.

Equivalent circuit model (ECM) techniques have been widely used to analyse the dynamic behaviour of battery voltage responses using resistor–capacitor (RC) elements [35]. Extensive studies have detailed the derivation of ECM models as well as experimental techniques for parameterisation [36]. Besides its use in online battery management applications, ECMs are commonly incorporated into thermal modelling to emulate bulk battery thermal behaviour under different cooling regimes at both cell level [37] and pack level [3]. Recent studies have also extended the application of ECMs to the prediction of temperature-related degradation [38]. A higher-order circuit representation of the cell comprises more RC parallel branches, which indicates more diverse transient behaviour and frequency response [39]. Depending on the battery form factor and chemistry, a higher-order ECM is generally more accurate yet susceptible to uncertainties [35]. Several studies have demonstrated that a 1-RC circuit provides considerable accuracy for NMC batteries during normal operation [40]; this was therefore adopted in the parameterisation study presented here.

This model is represented mathematically by the following equations [41]:

$$V_t = V_{oc} - R_0 I_L - V_p \tag{1}$$

$$\frac{dV_p}{dt} = -\frac{V_p}{R_p C_p} + \frac{I_L}{C_p} \tag{2}$$

where V_t denotes terminal voltage, V_{oc} open circuit voltage, R_0 internal resistance, R_p (imaginary) polarisation resistance, C_p polarisation capacitance, and I_L the circuit current.

ECM parameters were assumed to depend solely on SOC. R_0 was parameterised based on the HPPC results presented in Figure 7a. V_{oc} was obtained during a C/20 (2.7 A) discharge. As R_p does not possess a direct physical meaning and is a combined representation of different factors (e.g., charge transfer, ionic diffusion, temperature etc.), it is derived from empirical data to align the time constant of the ECM's response with the observed battery voltage response.

A lumped model does not fully represent the cell characteristics especially for large cell formats. However, since the battery exhibited minimal in-plane thermal gradients as discussed in Section 3.1, heat generation and rejection were treated as lumped parameters. The heat generation inside the battery was calculated based on Joule heating of internal resistance and polarisation resistance. The entropic heat was factored in R_p as a function of SOC. Effective thermal resistance has been employed by A. Persaran et al. to represent the heat exchange between the battery and the surrounding environment as a lumped parameter [42], which was adopted here to define the resistance of the test configuration to heat rejection. Therefore, the heat generation and heat rejection were formulated as follows:

$$Q_{gen}(t) = I^2(t)(R_0 + R_p) \tag{3}$$

$$Q_{dis}(t) = \frac{T(t) - T_{amb}(t)}{R_{eff}} \tag{4}$$

where T_{amb} denotes ambient temperature, T battery temperature, and R_{eff} the effective thermal resistance. T_{amb} was recorded as a temperature profile with the Bitrode cycler in the previous performance tests at 1 Hz.

The battery temperature was estimated based on the Bernardi equation as below [43]:

$$(t) = T(t-1) + \frac{Q(t-1)}{mC_{batt}} \tag{5}$$

$$Q(t) = Q_{gen}(t) + Q_{dis}(t) \tag{6}$$

where m denotes the mass of the battery, which is 0.75 kg, and C_{batt} is the battery specific heat capacity.

System thermal resistance was estimated in MATLAB 2025b with the empirical data of cell temperature and the respective current profile presented in Figures 3b and 5. A non-linear least square (LS) curve-fitting technique has been widely used in this field for robustness and simplicity. It is a regression-based optimisation method that minimises the sum of squared differences between measured and modelled battery voltage and impedance data. The curve fitting methodology is detailed in the study by Zhang et al. [31] and is therefore not discussed here. This technique was undertaken MATLAB using the "lsqcurvefit" function. The heat capacity for the cell was unknown; therefore, it was also adopted in the curve fitting with an assigned limit of 1–1.3 kJ/kgK to avoid over/under-estimating according to values reported in existing studies [44].

4.2. Simulation Results

The fitted effective thermal resistance under different cell clamping configurations and cooling environments is tabulated in Table 8. Schematic representations of R_{eff} for each clamping configuration are shown in Figure 9. The introduction of a Perspex clamping plate increased the resistance to heat rejection relative to the "Unclamp" configuration; therefore, the thermal resistance of the "Bespoke" clamping setup is between the "Unclamp" and "FullClamp" arrangements depending on the clamping area. For the "Bespoke"

arrangement, the fitted R_{eff} values were marginally higher in both ambient environment (0.07 K/W) and immersion cooling (0.03 K/W) compared to the "Unclamp" arrangement. Given that the "Bespoke" clamping plate covers approximately 30% of the pouch cell surface area, the fitted R_{eff} of "Bespoke" setup from empirical data is lower than the theoretical estimation based on the clamping area which corresponds to 1.53 K/W and 0.84 K/W in the ambient and immersion cooling environments. The difference between theoretical estimation and characterised result is expected as the effective resistance only includes the heat rejection through the large surface areas of the cell, where the battery tabs and the minor side areas (10% of the large side areas) also contributed to the overall heat dissipation, especially when submerged in the cooling fluid. This result suggests that the covered surface area from the "Bespoke" setup does not significantly impede heat rejection. In contrast, the "FullClamp" configuration led to an increase of 0.61 K/W and 0.4 K/W in thermal resistance in ambient and immersion cooling environments relative to the "Unclamp" arrangement. While immersion cooling significantly reduced the absolute thermal resistance by 0.84 K/W under the "FullClamp" configuration compared to "Unclamp" (0.63 K/W) and "Bespoke" (0.67 K/W) arrangements, the cell surfaces fully covered by Perspex sheets continued to contribute to substantially higher effective thermal resistance.

Table 8. Fitted effective thermal resistance.

R_{eff} (K/W)	Unclamp	FullClamp	Bespoke
Ambient	1.36	1.97	1.43
Immersion Cooling	0.73	1.13	0.76

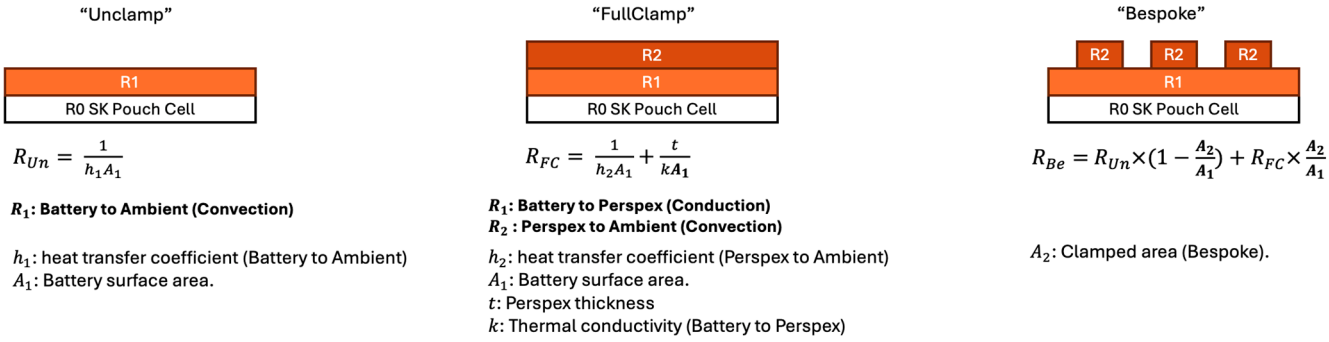


Figure 9. The schematic of thermal resistance under different cell clamping schemes.

Based on the breakdown of thermal resistance shown in Figure 9, the convective heat transfer coefficient h_1 is calculated from the estimated R_{Un} in the ambient environment, amounting 12.25 $W/(m^2K)$. This value aligns with the typical range reported for natural air convection (i.e., 1–10 $W/(m^2K)$ depending on air velocity [45]). This indicates that test cells had minimal impact on the ambient environment temperature within the thermal chamber (circa: 68 L in volume) during the performance tests. Conversely, the h_1 derived for immersion cooling (25.35 $W/(m^2K)$) is significantly lower than those reported in many previous studies (e.g., 2857.14 $W/(m^2K)$ reported by Han et al. [46]) due to the inclusion of battery intrinsic thermal resistance in our definition of R_{eff}. The derived coefficients are consistent with the expected thermal performance for the test cells. To investigate the fidelity of R_{eff} at elevated current loads, the current profiles shown in Figure 6b,c were used to simulate battery temperature rise following the modelling procedure described in Section 4.1.

A comparison between simulated and experimental temperature responses, together with mean squared error (MSE), is displayed in Figure 10. The error between simulation

and experimental data is further presented in Appendix A (Figure A1) for completeness. Across all test conditions, an increasing error was observed at higher C-rates, especially in the ambient environment. The cell clamping itself appears to have minimal influence on the simulation accuracy. While the simulated temperature rise generally agrees with the empirical data, the cool-down during the rest periods (i.e., t = 7–8 h, t = 11–12 h, and t = 14.5–16 h in Figure 10a,b indicate a slower heat rejection rate for the simulated cell temperature). The discrepancy is possibly influenced by the dynamic feedback control mechanisms of the thermal chamber operating at varying flow rates to maintain target test temperature. At elevated C-rates, increased heat release from the test cells may trigger higher air velocities in the thermal chamber or increased coolant flow rates in the immersion system to maintain the target test temperature of 25 °C, thereby enhancing convective heat transfer and accelerating temperature decay. These effects were not explicitly represented in the lumped thermal model. The error is less pronounced in the immersion cooling environment (maximum 3 °C) because of its greater thermal efficiency, whereas the error does exceed 10 °C after the 3C discharge event in the ambient environment. Additionally, the deviation in peak temperature may also arise from the reduced charge transfer resistance at elevated temperature, which further reduces heat generation and is not fully captured by the parameterisation process [11].

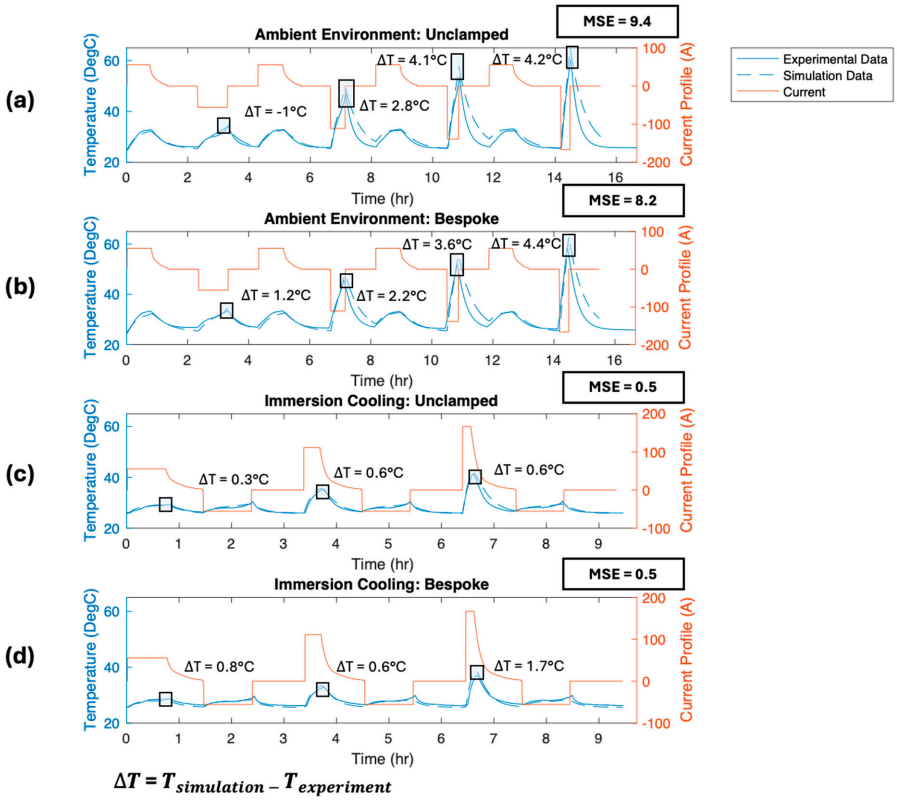


Figure 10. Simulated temperature rise corresponding to Figure 6: (**a**) "Unclamp" arrangement in the ambient environment; (**b**) "Bespoke" arrangement in the ambient environment; (**c**) "Unclamp" arrangement in the immersion cooling environment; (**d**) "Bespoke" arrangement in the immersion cooling environment.

In summary, the ECM parameterised using 1C discharge data provides a representative temperature rise at moderate C-rates. A more comprehensive parameterisation process incorporating empirical data across a broader range of C-rates and temperatures would potentially improve the simulation accuracy further. However, given the objective of this

work is to quantify the system thermal resistance, it is deemed to be beyond the scope of this initial study and is therefore addressed in Section 5.

5. Discussion

The results herein present a direct comparison of battery impedance responses and thermal behaviours between clamping schemes with different coverage areas. While homogeneous side pressure appears to be most effective in minimising cell impedance, redesigning the clamping geometry with reduced area enabled a trade-off between electrical performance and system-level heat rejection. The "Bespoke" clamping arrangement retained a substantial portion of the impedance-related benefits while mitigating the increase in system thermal resistance. The thermal and electrical benefits of the modified cell clamping scheme became more pronounced under effective cooling conditions and at higher C-rates. This orientates the application of cell clamping to batteries with high current loading duties (e.g., EV fast charging, acceleration, and regenerative breaking etc.). In addition, impedance characterisation of aged cells showed that the influence of side pressure on cell characteristics can become more significant with ageing, although the response varies between individual cells. The relevant mechanisms have been extensively reviewed by Li et al., [18], but this field still lacks sufficient experimental data to draw conclusive insights for Li-ion pouch/prismatic cells. More comprehensive studies on more pouch/prismatic cell models may provide additional insights as to the impact of cell clamping on battery at different stages of use, which may contribute to future energy storage system designs for batteries in second-life applications.

Lithium-ion batteries undergo reversible/irreversible volumetric change during electrical cycling, as previously identified in the literature. The application of partial clamping actively induces localised high pressure, which could further deviate from the unclamped areas during electrical cycling and induce localised physical fractures. It has been addressed that relatively low pressure is sufficient to push out the gaseous content and enhance the electrical contact between electrode layers [47]. While prominent studies have adopted a high clamping pressure of 310 kPa on large-format pouch cells under a homogenous clamping scheme [22], the exerted mechanical force of the battery needs to be deliberately considered to avoid damaging the cell in long-term cycling tests.

As the test cells chosen in this study have commercial relevance, the results provide useful insights into battery thermal behaviour at the cell level. While minimal in-plane thermal gradients were observed for an isolated cell under the present test conditions, thermal non-uniformity is expected to increase in densely packed modules, particularly for cells located away from direct cooling. Prior studies have shown that introducing additional metal bracing between cylindrical arrays can help mitigate spatial thermal gradients within the module [48]. Using this analogy, intercalating conductive clamping plates in a pouch cell module may offer a viable approach to simultaneously enhancing mechanical stability, electrical performance, and thermal uniformity. The design of the metallic plate correlates with the "Bespoke" arrangement introduced in this study. The results presented in this paper exhibit the positive influence of the cell clamping on battery characteristics and consequently its electrical and thermal performance in various cooling environments. However, the improvements were not optimal, as the "Bespoke" clamping plate primarily serves as an initial proof-of-concept design, which can be refined by optimising geometric design and material selection. A homogenous clamping plate design fabricated with a more conductive material (e.g., aluminium) will further improve the system's thermal resistance, although it will also increase cost and weight in the system. Therefore, future investigations on "Bespoke" clamping plate designs may lead to further enhanced system thermal behaviour with minimal setup.

A simplified 1-RC ECM coupled with a lumped thermal model was used to estimate battery temperature rise and system thermal resistance. As the "Bespoke" arrangement creates an uneven mechanical pressure on the test cells, the resultant cell impedance responses at local areas vary, which consequently affects local heat generation and in-plane heat conduction. We believe that the limitations of the lumped ECM approach can be overcome by discretising it into a thermal-node network consisting of numerous sub-ECMs, which allows the unclamped and clamped areas to be characterised and analysed separately. This would simplify the clamping plate iteration. As presented in the previous section, parameterisation using experimental data enabled reasonable estimation of the system thermal resistance and temperature rise prediction at moderate C-rates. However, increased deviations at higher C-rates indicate that thermal resistance characterised under a limited operating window may not be fully transferable across a wide range of currents and cooling conditions. In addition, the ECM parameters are commonly acknowledged as functions of both SOC and temperature, and the accuracy is compromised when simulating scenarios outside of the characterisation condition. We believe a more defined parameterisation process with empirical data obtained at various C-rates and test conditions (e.g., fixed air/coolant flow rate, temperature, etc.) would therefore improve the model accuracy and contribute to predicting battery thermal behaviour beyond the recommended C-rate.

The experimental methodology developed in this work is transferable to other pouch and prismatic cell formats, as the location of the cycle channel connection and spring-driven bolts can be adapted to different tab architectures. In addition, for batteries with higher silicon content within the anode, the swelling/contraction is more significant due to increased lithium intercalation capacity. It has been reported that the reversible swelling of a battery with 34 wt% SiO_x contents in the anode (i.e., 8%) is significantly higher than that of a graphite anode (i.e., 2%) at the beginning of life [49]. The significance of side pressure in this case would be more pronounced.

6. Conclusions

This study investigated the coupled effects of external cell clamping geometry and cooling strategy on the thermal and electrical behaviour of large-format lithium-ion pouch cells. By modifying the clamping area while maintaining a constant applied mechanical force, the trade-off between improved battery characteristics and impeded system heat rejection was quantified under both ambient and immersion cooling conditions.

For the commercial NMC pouch cell, minimal in-plane thermal gradients (1 °C) were observed on the uncovered pouch surface under natural convection. The incorporation of the "FullClamp" arrangement increased the overall cell temperature without amplifying in-plane thermal non-uniformity. In contrast, the "Bespoke" arrangement, which covers approximately 30% of the major pouch cell surfaces, demonstrated superior battery thermal behaviour and reduced battery temperature increase (0.5 °C at 1C in the ambient environment) compared to the "Unclamp" arrangement, whereas the "FullClamp" setup resulted in an increase of 1.2 °C. Consistent cell temperature hierarchies were observed under immersion cooling, where the "Bespoke" arrangement led to a further reduction in temperature rise by 0.9 °C at 1C. At 3C, the thermal benefits of the "Bespoke" arrangement became more pronounced, resulting in a reduction of 2 °C and 4.1 °C in the ambient and immersion cooling environments, respectively. These reductions coincided with improvements in electrical performance, including increases of 1.1 Ah in discharge capacity and 3.4 Ah in CC charged capacity at 3C.

The test cells were characterised with HPPC and EIS to quantify the causality between cell impedance response and the "Bespoke" arrangement. Despite the discrepancies in electrical connections of different cycles used for each technique, both results demonstrate that

the "FullClamp" arrangement is optimal in mitigating internal resistance, with an average 10.5% reduction at 10–100% SOC, as characterised by HPPC. The "Bespoke" arrangement achieved reduced improvement in comparison to "FullClamp", amounting to 3.6% in average. While the "FullClamp" arrangement did not seem to affect the charge transfer resistance characterised with EIS, the "Bespoke" arrangement increased it by 0.035 mΩ due to higher regional pressure. A greater deviation was seen on the aged SK pouch cells, where the "FullClamp" arrangement led to a reduction of 0.3–0.4 mΩ and 0.05–0.1 mΩ in internal resistance and charge transfer resistance, respectively. Similarly, the "Bespoke" arrangement exhibited a compromised enhancement of 0.05–0.25 mΩ and 0–0.1 mΩ, respectively. These results indicate that the influence of cell clamping on impedance is dependent on both clamping geometry and cell degradation state. A greater range of clamping area and clamping plate geometries are recommended for future studies to underpin the causality between cell impedance response and cell clamping arrangement design.

The experimental data were utilised to estimate system thermal resistance by using the curve-fitting technique in MATLAB. The result showed that "Bespoke" arrangement caused minimal increases of 0.07 K/W and 0.03 K/W in system thermal resistance in the ambient and immersion cooling environments compared to the "Unclamp" arrangement. This finding suggests that the reduced ohmic heating from the "Bespoke" arrangement outweighed the impeded system heat rejection, contributing to improved battery thermal behaviour. The estimated thermal resistances were employed to simulate battery temperature increase at higher C-rates. While the model provided representative temperature predictions at low and moderate C-rates, increased deviations at higher C-rates highlight the need for broader parameterisation across operating conditions in future studies.

Overall, the results demonstrate that optimising cell clamping geometry can mitigate thermal resistance associated with the mechanical constraint while retaining a substantial portion of the electrical and thermal benefits. The findings highlight the potential for further improvements in battery thermal behaviour by redesigning clamping plate geometry and/or selecting a material with higher thermal conductivity. This study also provides a practical framework for evaluating iterative clamping designs using simplified thermal-electrical modelling approaches.

Author Contributions: Conceptualisation, X.Z., J.M., G.P. and D.A.; methodology, X.Z.; formal analysis, X.Z.; investigation, X.Z.; writing—original draft preparation, X.Z.; writing—review and editing, X.Z., J.M., G.P. and D.A.; supervision—J.M.; funding acquisition, J.M., G.P. and D.A. All authors have read and agreed to the published version of the manuscript.

Funding: This research was supported by the EPSRC Industrial Cooperative Awards in Science & Technology (iCASE) with Castrol Limited at the University of Warwick, No. 2844646.

Data Availability Statement: The original contributions presented in the study are included in the article; further inquiries can be directed to the corresponding author.

Acknowledgments: This research was conducted within the Energy Innovation Centre (EIC) at WMG, University of Warwick, where we appreciate the technical support from the battery lab teams.

Conflicts of Interest: The authors declare that they have no known competing financial interests or personal relationships that could have appeared to influence the work reported in this paper. Authors Giles Prentice and David Ainsworth were employed by the company Castrol Limited, which provided funding support for the work.

Abbreviations

The following abbreviations are used in this manuscript:

EV	Electric Vehicle

ICE	Internal Combustion Engine
ECM	Equivalent Circuit Model
BTMS	Battery Thermal Management System
CC	Constant Current
CV	Constant Voltage
HPPC	Hybrid Power Pulse Characterisation
EIS	Electrochemical Impedance Spectroscopy
MSE	Mean Squared Error
LS	Least Square
RC	Resistor–Capacitor
SOC	State of Charge
V_t	Terminal Voltage (V)
V_{oc}	Open Circuit Voltage (V)
R_0	Internal Resistance (Ω)
R_p	Polarisation Resistance (Ω)
I_L	Current (A)
V_p	Polarisation Voltage (V)
C_p	Polarisation Capacitance (C)
Q_{gen}	Generated Heat (kJ)
Q_{dis}	Dissipated Heat (kJ)
R_{eff}	Effective Thermal Resistance (K/W)
T_{amb}	Ambient Temperature (°C)
T	Battery Temperature (°C)
C_{batt}	Battery Heat Capacity (J/kgK)
m	Mass (kg)
h	Heat Transfer Coefficient ($W/(m^2K)$)
A	Convection Area (m^2)

Appendix A

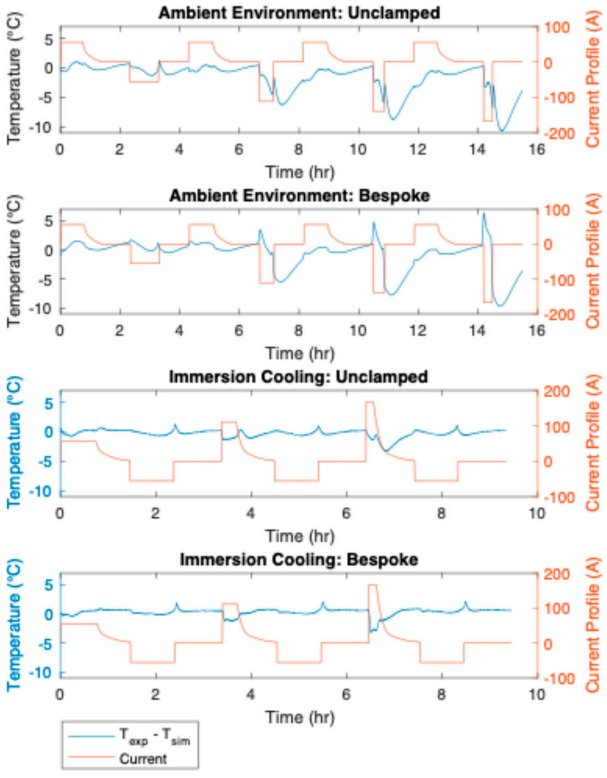


Figure A1. Error between simulation and experimental results corresponding to Figure 10.

References

1. Veza, I.; Asy'ari, M.Z.; Idris, M.; Epin, V.; Rizwanul Fattah, I.M.; Spraggon, M. Electric vehicle (EV) and driving towards sustainability: Comparison between EV, HEV, PHEV, and ICE vehicles to achieve net zero emissions by 2050 from EV. *Alex. Eng. J.* **2023**, *82*, 459–467. [CrossRef]
2. Roe, C.; Feng, X.; White, G.; Li, R.; Wang, H.; Rui, X.; Li, C.; Zhang, F.; Null, V.; Parkes, M.; et al. Immersion cooling for lithium-ion batteries–A review. *J. Power Sources* **2022**, *525*, 231094. [CrossRef]
3. Zhao, Y.; Patel, Y.; Zhang, T.; Offer, G.J. Modeling the Effects of Thermal Gradients Induced by Tab and Surface Cooling on Lithium Ion Cell Performance. *J. Electrochem. Soc.* **2018**, *165*, A3169–A3178. [CrossRef]
4. Chen, D.; Jiang, J.; Kim, G.-H.; Yang, C.; Pesaran, A. Comparison of different cooling methods for lithium ion battery cells. *Appl. Therm. Eng.* **2016**, *94*, 846–854. [CrossRef]
5. Waldmann, T.; Wilka, M.; Kasper, M.; Fleischhammer, M.; Wohlfahrt-Mehrens, M. Temperature dependent ageing mechanisms in Lithium-ion batteries–A Post-Mortem study. *J. Power Sources* **2014**, *262*, 129–135. [CrossRef]
6. Birkl, C.R.; Roberts, M.R.; McTurk, E.; Bruce, P.G.; Howey, D.A. Degradation diagnostics for lithium ion cells. *J. Power Sources* **2017**, *341*, 373–386. [CrossRef]
7. Shen, W.; Wang, N.; Zhang, J.; Wang, F.; Zhang, G. Heat Generation and Degradation Mechanism of Lithium-Ion Batteries during High-Temperature Aging. *ACS Omega* **2022**, *7*, 44733–44742. [CrossRef]
8. Zhang, S.S.; Xu, K.; Jow, T.R. Optimization of the forming conditions of the solid-state interface in the Li-ion batteries. *J. Power Sources* **2004**, *130*, 281–285. [CrossRef]
9. Ma, S.; Jiang, M.; Tao, P.; Song, C.; Wu, J.; Wang, J.; Deng, T.; Shang, W. Temperature effect and thermal impact in lithium-ion batteries: A review. *Prog. Nat. Sci. Mater. Int.* **2018**, *28*, 653–666. [CrossRef]
10. Lazanas, A.C.; Prodromidis, M.I. Electrochemical Impedance Spectroscopy—A Tutorial. *ACS Meas. Sci. Au* **2023**, *3*, 162–193. [CrossRef]
11. Lei, S.; Bojun, T.; Huaiyu, L.; Chunfeng, Z.; Xiaojun, Z. Static method of liquid-immersed thermal regulation for a household energy-storing with lithium-ion batteries. *Energy Build.* **2025**, *347*, 116325. [CrossRef]
12. Sheng, L.; Zhang, H.; Su, L.; Zhang, Z.; Zhang, H.; Li, K.; Fang, Y.; Ye, W. Effect analysis on thermal profile management of a cylindrical lithium-ion battery utilizing a cellular liquid cooling jacket. *Energy* **2021**, *220*, 119725. [CrossRef]
13. He, H.; Fly, A.; Barbour, E.; Chen, X. Numerical investigation of module-level inhomogeneous ageing in lithium-ion batteries from temperature gradients and electrical connection topologies. *Commun. Eng.* **2024**, *3*, 89. [CrossRef]
14. Zhan, C.; Wu, T.; Lu, J.; Amine, K. Dissolution, Migration, and Deposition of Transition Metal Ions in Li-ion Batteries Exampled by Mn-based cathodes—A Critical Review. *Energy Environ. Sci.* **2017**, *11*, 243–257. [CrossRef]
15. Lin, X.; Khosravinia, K.; Hu, X.; Li, J.; Lu, W. Lithium Plating Mechanism, Detection, and Mitigation in Lithium-Ion Batteries. *Prog. Energy Combust. Sci.* **2021**, *87*, 100953. [CrossRef]
16. Müller, V.; Scurtu, R.-G.; Richter, K.; Waldmann, T.; Memm, M.; Danzer, M.A.; Wohlfahrt-Mehrens, M. Effects of Mechanical Compression on the Aging and the Expansion Behavior of Si/C-Composite | NMC811 in Different Lithium-Ion Battery Cell Formats. *J. Electrochem. Soc.* **2019**, *166*, A3796–A3805. [CrossRef]
17. Barai, A.; Tangirala, R.; Uddin, K.; Chevalier, J.; Guo, Y.; McGordon, A.; Jennings, P. The effect of external compressive loads on the cycle lifetime of lithium-ion pouch cells. *J. Energy Storage* **2017**, *13*, 211–219. [CrossRef]
18. Li, R.; Li, W.; Singh, A.; Ren, D.; Hou, Z.; Ouyang, M. Effect of external pressure and internal stress on battery performance and lifespan. *Energy Storage Mater.* **2022**, *52*, 395–429. [CrossRef]
19. Müller, V.; Scurtu, R.-G.; Memm, M.; Danzer, M.A.; Wohlfahrt-Mehrens, M. Study of the influence of mechanical pressure on the performance and aging of Lithium-ion battery cells. *J. Power Sources* **2019**, *440*, 227148. [CrossRef]
20. Mussa, A.S.; Klett, M.; Lindbergh, G.; Lindström, R.W. Effects of external pressure on the performance and ageing of single-layer lithium-ion pouch cells. *J. Power Sources* **2018**, *385*, 18–26. [CrossRef]
21. Berckmans, G.; De Sutter, L.; Marinaro, M.; Smekens, J.; Jaguemont, J.; Wohlfahrt-Mehrens, M.; Van Mierlo, J.; Omar, N. Analysis of the effect of applying external mechanical pressure on next generation silicon alloy lithium-ion cells. *Electrochim. Acta* **2019**, *306*, 387–395. [CrossRef]
22. Du, X.; Hu, Y.; Choe, S.-Y.; Garrick, T.R.; Fernandez, M.A. Characterization and analysis of the effect of pressure on the performance of a large format NMC/C lithium-ion battery. *J. Power Sources* **2023**, *573*, 233117. [CrossRef]
23. Zhang, X.; Marco, J.; Prentice, G.; Ainsworth, D. Incorporating Cell Clamping and the Impact on Lithium-Ion Pouch Cell Performance. In *Proceedings of the 2025 IEEE/AIAA Transportation Electrification Conference and Electric Aircraft Technologies Symposium (ITEC+EATS), Anaheim, CA, USA, 18-20 June 2025*; IEEE: Anaheim, CA, USA, 2025; pp. 1–6.
24. Dileep, H.; Jha, K.K.; Mahapatra, P.S.; Pattamatta, A. Thermal characterization of pouch cell using infrared thermography and electrochemical modelling for the Design of Effective Battery Thermal Management System. *Appl. Energy* **2024**, *376*, 124301. [CrossRef]

25. Grandjean, T.; Barai, A.; Hosseinzadeh, E.; Guo, Y.; McGordon, A.; Marco, J. Large format lithium ion pouch cell full thermal characterisation for improved electric vehicle thermal management. *J. Power Sources* **2017**, *359*, 215–225. [CrossRef]
26. Zhang, A.; Li, Y. Thermal Conductivity of Aluminum Alloys—A Review. *Materials* **2023**, *16*, 2972. [CrossRef]
27. Assael, M.J.; Botsios, S.; Gialou, K.; Metaxa, I.N. Thermal Conductivity of Polymethyl Methacrylate (PMMA) and Borosilicate Crown Glass BK7. *Int. J. Thermophys.* **2005**, *26*, 1595–1605. [CrossRef]
28. Hagen, M.; Dörfler, S.; Fanz, P.; Berger, T.; Speck, R.; Tübke, J.; Althues, H.; Hoffmann, M.J.; Scherr, C.; Kaskel, S. Development and costs calculation of lithium–sulfur cells with high sulfur load and binder free electrodes. *J. Power Sources* **2013**, *224*, 260–268. [CrossRef]
29. Mazur, P.; Mrlik, J.; Pocedic, J.; Vrana, J.; Dundalek, J.; Kosek, J.; Bystron, T. Effect of graphite felt properties on the long-term durability of negative electrode in vanadium redox flow battery. *J. Power Sources* **2019**, *414*, 354–365. [CrossRef]
30. Białoń, T.; Niestrój, R.; Skarka, W.; Korski, W. HPPC Test Methodology Using LFP Battery Cell Identification Tests as an Example. *Energies* **2023**, *16*, 6239. [CrossRef]
31. Zhang, Y.; Liu, Z.; Sun, X.; An, Y.; Zhang, X.; Wang, K.; Dong, C.; Huo, Q.; Wei, T.; Ma, Y. Experimental study of thermal charge–discharge behaviors of pouch lithium-ion capacitors. *J. Energy Storage* **2019**, *25*, 100902. [CrossRef]
32. Bolsinger, C.; Zorn, M.; Birke, K.P. Electrical contact resistance measurements of clamped battery cell connectors for cylindrical 18650 battery cells. *J. Energy Storage* **2017**, *12*, 29–36. [CrossRef]
33. Barai, A.; Uddin, K.; Dubarry, M.; Somerville, L.; McGordon, A.; Jennings, P.; Bloom, I. A comparison of methodologies for the non-invasive characterisation of commercial Li-ion cells. *Prog. Energy Combust. Sci.* **2019**, *72*, 1–31. [CrossRef]
34. Cannarella, J.; Arnold, C.B. Ion transport restriction in mechanically strained separator membranes. *J. Power Sources* **2013**, *226*, 149–155. [CrossRef]
35. Hu, X.; Li, S.; Peng, H. A comparative study of equivalent circuit models for Li-ion batteries. *J. Power Sources* **2012**, *198*, 359–367. [CrossRef]
36. Zhang, C.; Allafi, W.; Dinh, Q.; Ascencio, P.; Marco, J. Online estimation of battery equivalent circuit model parameters and state of charge using decoupled least squares technique. *Energy* **2018**, *142*, 678–688. [CrossRef]
37. Karimi, D.; Behi, H.; Berecibar, M.; Van Mierlo, J. A comprehensive coupled 0D-ECM to 3D-CFD thermal model for heat pipe assisted-air cooling thermal management system under fast charge and discharge. *Appl. Energy* **2023**, *339*, 120987. [CrossRef]
38. Li, S.; Zhang, C.; Zhao, Y.; Offer, G.J.; Marinescu, M. Effect of thermal gradients on inhomogeneous degradation in lithium-ion batteries. *Commun. Eng.* **2023**, *2*, 74. [CrossRef]
39. Luo, K.; Chen, X.; Zheng, H.; Shi, Z. A review of deep learning approach to predicting the state of health and state of charge of lithium-ion batteries. *J. Energy Chem.* **2022**, *74*, 159–173. [CrossRef]
40. Tran, M.-K.; DaCosta, A.; Mevawalla, A.; Panchal, S.; Fowler, M. Comparative Study of Equivalent Circuit Models Performance in Four Common Lithium-Ion Batteries: LFP, NMC, LMO, NCA. *Batteries* **2021**, *7*, 51. [CrossRef]
41. Auger, D.J.; Fotouhi, A.; Propp, K.; Longo, S. Battery Management Systems–State Estimation for Lithium–Sulfur Batteries. In *Lithium–Sulfur Batteries*; Wild, M., Offer, G.J., Eds.; Wiley: Hoboken, NJ, USA, 2019; pp. 249–272. ISBN 978-1-119-29789-5.
42. Pesaran, A.A. Battery thermal models for hybrid vehicle simulations. *J. Power Sources* **2002**, *110*, 377–382. [CrossRef]
43. Jindal, P.; Katiyar, R.; Bhattacharya, J. Evaluation of accuracy for Bernardi equation in estimating heat generation rate for continuous and pulse-discharge protocols in LFP and NMC based Li-ion batteries. *Appl. Therm. Eng.* **2022**, *201*, 117794. [CrossRef]
44. Bryden, T.S.; Dimitrov, B.; Hilton, G.; Ponce De León, C.; Bugryniec, P.; Brown, S.; Cumming, D.; Cruden, A. Methodology to determine the heat capacity of lithium-ion cells. *J. Power Sources* **2018**, *395*, 369–378. [CrossRef]
45. Allafi, W.; Zhang, C.; Uddin, K.; Worwood, D.; Dinh, T.Q.; Ormeno, P.A.; Li, K.; Marco, J. A lumped thermal model of lithium-ion battery cells considering radiative heat transfer. *Appl. Therm. Eng.* **2018**, *143*, 472–481. [CrossRef]
46. Han, J.-W.; Garud, K.S.; Hwang, S.-G.; Lee, M.-Y. Experimental Study on Dielectric Fluid Immersion Cooling for Thermal Management of Lithium-Ion Battery. *Symmetry* **2022**, *14*, 2126. [CrossRef]
47. Deich, T.; Storch, M.; Steiner, K.; Bund, A. Effects of module stiffness and initial compression on lithium-ion cell aging. *J. Power Sources* **2021**, *506*, 230163. [CrossRef]
48. Cha, H.-R.; Angani, A.; Hwang, M.-H. Thermal management of lithium-ion batteries by novel designs of wavy cold plates: Performance comparison. *J. Energy Storage* **2023**, *73*, 109303. [CrossRef]
49. Von Kessel, O.; Avdyli, A.; Vrankovic, D.; Birke, K.P. Swelling, pressure evolution and aging in high-silicon/ graphite composite lithium-ion batteries. *J. Power Sources* **2024**, *610*, 234582. [CrossRef]

Disclaimer/Publisher's Note: The statements, opinions and data contained in all publications are solely those of the individual author(s) and contributor(s) and not of MDPI and/or the editor(s). MDPI and/or the editor(s) disclaim responsibility for any injury to people or property resulting from any ideas, methods, instructions or products referred to in the content.